UC Davis
UC Davis Previously Published Works

Title
Selectivity filter modalities and rapid inactivation of the hERG1 channel

Permalink
https://escholarship.org/uc/item/6d06g7nk

Journal
Proceedings of the National Academy of Sciences of the United States of America, 117(6)

ISSN
0027-8424

Authors
Miranda, Williams E
DeMarco, Kevin R
Guo, Jiqing
et al.

Publication Date
2020-02-11

DOI
10.1073/pnas.1909196117

Peer reviewed

eScholarship.org Powered by the California Digital Library
University of California

Selectivity filter modalities and rapid inactivation of the hERG1 channel

Williams E. Miranda[a], Kevin R. DeMarco[b], Jiqing Guo[c], Henry J. Duff[c], Igor Vorobyov[b,d], Colleen E. Clancy[b,d,1], and Sergei Yu. Noskov[a,1]

[a]Centre for Molecular Simulation, Department of Biological Sciences, University of Calgary, Calgary, AB T2N 1N4, Canada; [b]Department of Physiology and Membrane Biology, University of California, Davis, CA 95616; [c]Libin Cardiovascular Institute of Alberta, Cumming School of Medicine, University of Calgary, Calgary, AB T2N 4N1, Canada; and [d]Department of Pharmacology, University of California, Davis, CA 95616

Edited by Michael L. Klein, Temple University, Philadelphia, PA, and approved December 19, 2019 (received for review May 28, 2019)

The human *ether-á-go-go*–related gene (hERG1) channel conducts small outward K^+ currents that are critical for cardiomyocyte membrane repolarization. The gain-of-function mutation N629D at the outer mouth of the selectivity filter (SF) disrupts inactivation and K^+-selective transport in hERG1, leading to arrhythmogenic phenotypes associated with long-QT syndrome. Here, we combined computational electrophysiology with Markov state model analysis to investigate how SF-level gating modalities control selective cation transport in wild-type (WT) and mutant (N629D) hERG1 variants. Starting from the recently reported cryogenic electron microscopy (cryo-EM) open-state channel structure, multiple microseconds-long molecular-dynamics (MD) trajectories were generated using different cation configurations at the filter, voltages, electrolyte concentrations, and force-field parameters. Most of the K^+ permeation events observed in hERG1-WT simulations occurred at microsecond timescales, influenced by the spontaneous dehydration/rehydration dynamics at the filter. The SF region displayed conductive, constricted, occluded, and dilated states, in qualitative agreement with the well-documented flickering conductance of hERG1. In line with mutagenesis studies, these gating modalities resulted from dynamic interaction networks involving residues from the SF, outer-mouth vestibule, P-helices, and S5–P segments. We found that N629D mutation significantly stabilizes the SF in a state that is permeable to both K^+ and Na^+, which is reminiscent of the SF in the nonselective bacterial NaK channel. Increasing the external K^+ concentration induced "WT-like" SF dynamics in N629D, in qualitative agreement with the recovery of flickering currents in experiments. Overall, our findings provide an understanding of the molecular mechanisms controlling selective transport in K^+ channels with a nonconventional SF sequence.

ion channels | molecular dynamics | human ether-á-go-go channel | long-QT syndrome

The human *ether-á-go-go*–related gene (*hERG1* or *KCNH2*) encodes the pore-forming subunit of the hERG1 potassium-selective channel (K^+:Na^+ ~ 100:1), also known as $K_V11.1$ (1). This channel is responsible for the rapidly activating delayed-rectifier current (I_{Kr}) involved in cardiomyocyte membrane repolarization after a cardiac action potential (CAP) upstroke, preventing arrhythmogenic premature depolarizations (2). The distinctively rapid inactivation during membrane depolarization makes the hERG1 channel behave as a typical inward rectifier (3–7). The subsequent loss of K^+ permeation through the hERG1 channel enables a long plateau phase, which is one of the hallmark features of the CAP. Inherited loss-of-function mutations in hERG1 that disrupt I_{Kr} can result in long-QT syndrome (LQTS) and an increased risk of developing cardiac arrhythmias and sudden death (8–14). Unlike most of the well-studied K^+-selective channels, hERG1 contains a nonconventional selectivity filter (SF) sequence, in which a phenylalanine replaces the canonical tyrosine residue (*GFG* in hERG1 vs. *GYG* in most K^+ channels). This replacement may explain the striking difference between the flickering current conducted by hERG1 (3–7) and the slow-inactivating current observed from its bacterial counterparts (15–17) and voltage-gated channels from the Shaker family (18–20). Moreover, the electrophysiological properties of the hERG1 channel are highly sensitive to mutations altering local electrical fields or changing the interaction network topology in the vicinity of canonical K^+ binding sites in the SF region. For example, the mutation N629D adjacent to the SF signature sequence $_{626}GFG_{628}$ of the hERG1 channel was the first reported to produce LQTS through a gain-of-function phenotype (11). Indeed, this substitution has been reported as either a "loss-of-function" mutation related to decreased current density, mediated in part by a defect in trafficking the tetramers to the plasma membrane (21), or a "gain-of-function" mutation due to the striking altered selectivity and apparent loss of C-type inactivation (22).

In contrast to hERG1 wild type (WT), this mutant conducts steady, nonselective or only weakly selective cation currents (K^+:Na^+ ~ 3:2) (22). It was proposed that inward I_{Na^+} enabled by the hERG1-N629D variant replaces the outward repolarizing I_{K^+}, leading to severe aberration in heart rhythm and teratogenic effects (22, 23). Interestingly, the altered phenotype can be corrected in vitro by exposure of the N629D mutant to transient increases in the external K^+ concentration ([K^+]) (24). The arrhythmogenic gain-of-function phenotype induced by a single-residue substitution and its reversion by an increase in external [K^+] are suggestive of a very dynamic SF in the hERG1 channel. This may represent a general feature for flickering ion channels with small conductance such as hERG1 and related hyperpolarization-activated cyclic nucleotide–gated (HCN) channels.

Significance

The familial mutations impacting repolarization K^+ currents conducted by the hERG1 channel are significant determinants of arrhythmogenicity. Here, we show how the arrhythmogenic gain-of-function mutation (N629D) in the pore domain impairs channel selectivity and inactivation by shifting complex conformational equilibria between the conductive and nonconductive states of the selectivity filter and by impacting filter modalities. This study highlights notable differences in the permeation and inactivation dynamics in a human channel that displays a nonconventional selectivity filter.

Author contributions: H.J.D., I.V., C.E.C., and S.Y.N. designed research; W.E.M., K.R.D., and S.Y.N. performed research; J.G. and S.Y.N. contributed new reagents/analytic tools; W.E.M., K.R.D., J.G., I.V., and S.Y.N. analyzed data; and W.E.M., K.R.D., H.J.D., I.V., C.E.C., and S.Y.N. wrote the paper.

The authors declare no competing interest.

This article is a PNAS Direct Submission.

Published under the PNAS license.

[1]To whom correspondence may be addressed. Email: ceclancy@ucdavis.edu or snoskov@ucalgary.ca.

This article contains supporting information online at https://www.pnas.org/lookup/suppl/doi:10.1073/pnas.1909196117/-/DCSupplemental.

First published January 24, 2020.

The molecular mechanisms controlling flickering and selective permeation in hERG1-WT and the loss/recovery of inactivation and selectivity in hERG1-N629D are yet to be established. A feasible mechanism was proposed recently from the combined experimental and modeling study of ion transport across the bacterial K^+-channel KcsA (25). The distinct structural states or "modalities" of the SF were prompted by the flipping dynamics of carbonyl oxygens lining the cation permeation pathway. The carbonyl flipping away from the central permeation axis destabilizes cation binding and disrupts the permeation-competent state of the SF. These dynamic modalities were also proposed to act as precursors for the formation of C-type inactivated state(s) in hERG1 (25). The determination of the full structure of the hERG1 channel in its open sate using cryogenic electron microscopy (cryo-EM) (3.8 Å resolution; Protein Data Bank [PDB] ID code 5VA2) (26) shows that the *GFG* sequence found in KCNH2 channel does not disrupt the canonical configuration of the SF region (27), with carbonyl oxygens forming the canonical binding sites S0–S4 (Fig. 1 *A* and *B*). This structure, presumably, represents a depolarized (open) state of the pore domain and allows direct studies of interconnection between the gating modalities of the SF region and selective ion transport in hERG1 variants.

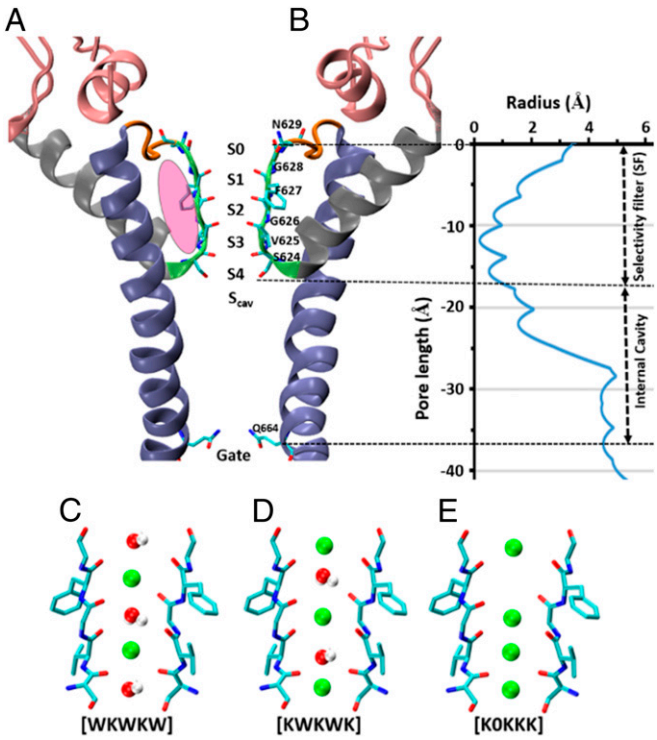

Fig. 1. Pore domain (PD) of the hERG1 channel. (*A*) Structural representation. The S5–P segments, P-helices, SF, outer-mouth vestibule, and S6 helices are highlighted in pink, silver, green, orange, and violet colors, respectively. Only two monomers are shown for clarity. The S5 helices of the PD were omitted for the same reason. The residues from the SF ($_{624}$SVGFG$_{628}$), N629 from the vestibule, and Q664 from the cytoplasmic gate are highlighted in licorice representation. The N, C, and O atoms are colored in blue, cyan, and red colors, respectively. The labels S0–S_{cav} indicate potassium or water SF binding sites. The pink shaded area indicates the region behind the filter for one of the monomers. (*B*) Radius profile along the pore domain. (*C*–*E*) Initial ion configurations at the SF used in our MD simulations. The symbols K, W, and 0 indicate potassium ions, water, and vacancy, respectively, at the SF binding sites S0–S4. A third ion was placed in S_{cav} binding site for the configuration shown in *C*. This configuration was also used for placing Na^+ ions.

Here, we combined computational-electrophysiology approaches (28) with all-atom molecular-dynamics (MD) simulations and Markov state model (MSM) analysis (29, 30) to investigate the molecular mechanisms underpinning SF dynamics and cation permeation (K^+, Na^+) in hERG1-WT and hERG1-N629D. Starting from the open-state channel structure (26), we generated multiple 2- to 4-μs-long trajectories for each channel variant for different permeant cations (K^+, Na^+), applied voltages, and [electrolyte] = 150 and 500 mM (here considered as low and high, respectively). We observed multiple K^+ permeation events through the hERG1-WT filter alternating with latent (nonconducting) periods, influenced by structural distortions at the SF. This region of the pore displayed metastable states including collapse, dilation, and occlusion that resulted in dehydration of several binding sites. Transient filter dilation and rehydration events enabled permeant ions access to the filter, restoring the permeation-competent state of the channel. This SF-level conformational cycle is in line with well-known flickering K^+ currents present in hERG1. The direct involvement of the structural motifs around the SF in permeation control provides molecular-level explanation for several deleterious mutations located in the outer-mouth vestibule, P-helix, and S5–P segments. The most populated metastable state for the gain-of-function hERG1-N629D variant shows structural disruption of the canonical SF configuration found in all families of K^+ channels, resulting in a fully hydrated and dilated vestibule at the sites S0–S2 while retaining sites S3 and S4. This SF configuration, reminiscent of nonselective NaK channels, is considerably more stable than the SF in hERG1-WT and allows permeation of K^+ and Na^+ ions. This explains the loss of both inactivation and selectivity in hERG1-N629D.

Results

Stability of the hERG1-WT Open-State Cryo-EM Structure. To test the stability of the recently reported open-state structure of the transmembrane region of the hERG1-WT channel (26) (*SI Appendix*, Fig. S1), we performed an unbiased 2-μs-long MD simulation (*SI Appendix*, Table S1). The root-mean-square deviations (RMSDs) plateaued at ∼2, 3, and 7 Å for the backbone atoms from the pore, cytoplasmic, and voltage-sensing domains (VSDs), respectively (*SI Appendix*, Fig. S2*A*). The overall fold of each transmembrane helix from the VSDs is mostly preserved (*SI Appendix*, Fig. S2 *B* and *C*). Furthermore, the residues K525, R528, and R531 [major contributors to the gating charge (31)] kept their positions relative to F463, the putative charge transfer center in hERG1 (*SI Appendix*, Fig. S2 *D* and *E*). This indicates that the VSDs maintained the depolarized configuration reported in the cryo-EM structure (26), despite relaxation observed in the MD simulation. It is worth noting that the VSDs have shown to have very "loose" packing and significant conformational plasticity in experiments (32, 33). In contrast, the pore domain (PD) is the most stable structural element (*SI Appendix*, Fig. S2*A*) in line with MD simulations of bacterial and mammalian K^+ channels (34, 35). Consequently, the intracellular gate remains open (*SI Appendix*, Fig. S2 *F* and *G*), and the internal cavity is well hydrated during the simulation (57 ± 8 water molecules).

Permeability of hERG1 Variants in Voltage-Applied Simulations. We considered different ion configurations and force-fields with and without nonbonded fix (NBFIX) corrections (*SI Appendix*, Table S1), in order to test the importance of different factors mapped out in various studies of K^+-selective channels in the literature. For instance, the starting [WKWKW] and [KWKWK] configurations (Fig. 1 *C* and *D*) are to match potassium binding sites emphasized in the "water-mediated" or "soft" knock-on permeation mechanism (36–40). The [K0KKK] configuration (Fig. 1*E*) resembles the most populated SF state reported in the direct or "hard" knock-on mechanism (41). The version of Lennard–Jones

Table 1. Average occupancy of water molecules at specific regions of hERG1 variants in simulations using [K^+] = 150 mM, V = 750 mV, and the NBFIX correction

Initial configuration	Inside SF WT/N629D	Behind SF* WT/N629D	Internal cavity WT/N629D
[WKWKW]	1 ± 1/5 ± 1	3 ± 1/0 ± 0	76 ± 8/62 ± 8
[KWKWK]	2 ± 1/3 ± 1	3 ± 1/1 ± 3E-1	63 ± 5/83 ± 10
[K0KKK]	3 ± 2/4 ± 3	2 ± 1/1 ± 1E-1	91 ± 11/61 ± 6

*Average over the four monomers.

(LJ) parameters known as the NBFIX correction (*SI Appendix*, Table S1) has been crucial for accurate modeling of filter hydration, ion–ion correlations, and the permeation process (42–45).

hERG1-WT. The MD simulations with applied electrical field show on average less hydration inside the SF (Table 1) compared to the unbiased simulation (4 ± 1 water molecules). This may result from the biasing effect of the applied voltage on the permeation of particles (water, ions) through the SF region. Although the internal cavity remains hydrated along the trajectories (Table 1), with the intracellular gate of the channel open and accessible to permeant cations, we only observed full K^+ permeation events in simulations under the high bias conditions (750 mV) combined with the NBFIX parameters (*SI Appendix*, *Supplementary Results*). A high-field regime chosen in this study has been reported to best approximate the experimentally measured conductance in Shaker channel (46).

We recorded four water-mediated K^+ permeation events that included the cations initially placed in the [WKWKW] configuration, plus another K^+ that permeated from the intracellular side of the channel in the first tens of nanoseconds (Fig. 2 *A*, *Inset*, and Movie S1). This is reminiscent of the soft knock-on permeation mechanism (36–40). However, following SF distortion and dewetting at $t \sim 50$ ns (*SI Appendix*, Fig. S3 *A* and *B*), incoming cations displayed multiple and stable (microsecond-long) binding events to sites S_{cav} and S4 (Fig. 2*A*). Six additional water-mediated permeation events alternated with latent (nonconducting) periods that could last from hundreds of nanoseconds to more than 1 μs along the ∼4-μs trajectory (Fig. 2*A* and Movie S1). A similar permeation mechanism was observed for the shorter [KWKWK] and [K0KKK] simulations (∼2.5 μs each), which displayed seven and eight water-mediated permeation events, respectively, after SF distortion and dewetting at $t \sim 50$ ns (*SI Appendix*, Fig. S4 *A* and *B*). Notably, we observed a spontaneous hydration of the filter that disrupted direct K^+–K^+ interactions in the [K0KKK] configuration (Table 1). Increasing [KCl] to 500 mM only resulted in eight permeation events during ∼4 μs (*SI Appendix*, Fig. S4*C*). By averaging among all permeation events observed from [WKWKW], [KWKWK], and [K0KKK] simulations performed using low [K^+], V = 750 mV, and the NBFIX correction, we estimated an outward conductance value of ∼0.8 ± 0.2 pS for hERG1-WT. This small conductance is expected from the low K^+ occupancy observed at the SF (1 ± 1 cations) in each simulation. In contrast, no inward Na^+ permeation events were observed for this channel variant in the simulation performed using [Na^+] = 150 mM and V = −750 mV (*SI Appendix*, Table S1 and *Supplementary Results*). These findings are in fair agreement with the flickering and small K^+-selective outward conductance (3 to 5 pS) reported for hERG1-WT in the open state from experiments (2–5, 7).

hERG1-N629D. The mutant shows on average more hydration inside the SF than in the WT (Table 1). The internal cavity also remains hydrated and accessible to cations in the simulations with applied electrical field (Table 1). Nevertheless, only four water-mediated permeation events were observed in [WKWKW] simulation (∼4 μs long) (Fig. 2*B* and Movie S2), which showed restricted dynamics at the SF (*SI Appendix*, Fig. S3 *C* and *D*). The cations mostly accumulated at site S3 for more than 1 μs before exiting toward the extracellular side of the channel (Fig. 2*B*). Consequently, the K^+ occupancy at the SF was low (1 ± 1 cations). A low K^+ occupancy of 1 ± 1 mostly at sites S2, S3, or S4 was also observed for the simulations started with the ion configurations [KWKWK] and [K0KKK] (∼2.5 μs long each), for which 10 and 4 permeation events were recorded, respectively (*SI Appendix*, Fig. S5 *A* and *B*). These permeation events were separated by latent (nonconducting) periods that could last from hundreds of nanoseconds to ∼1 μs (*SI Appendix*, Fig. S5 *A* and *B*). We also

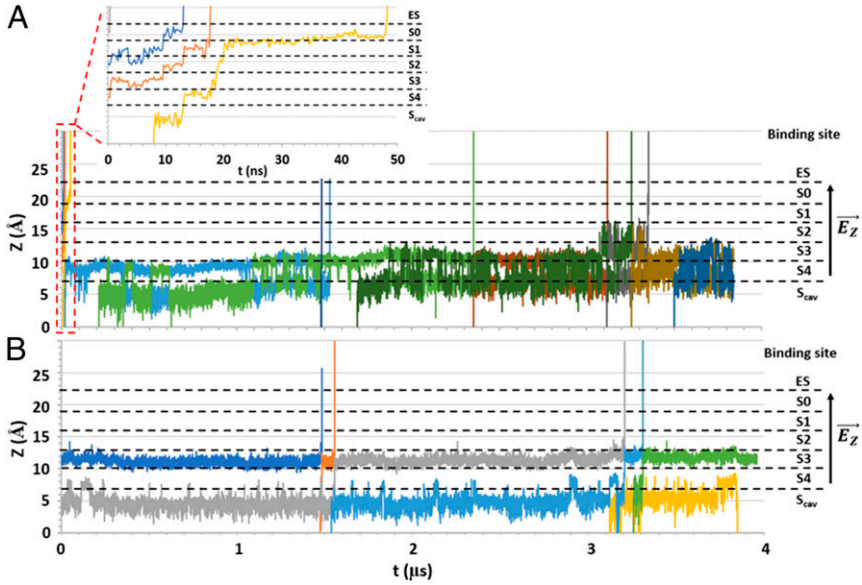

Fig. 2. Potassium cation permeation events observed for hERG1 variants. (*A*) WT and (*B*) N629D. For each channel variant, the simulations were performed using the initial ion configuration [WKWKW], [K^+] = 150 mM, V = 750 mV, and the NBFIX correction. Permeant cations are represented by different colors for each system. The binding sites at the SF along the pore axis are indicated by dashed lines. The acronym **ES** indicates the extracellular side of the channel. The black arrow indicates the direction of the applied electric field. The *Inset* in *A* zooms into the permeation events during the first 50 ns of the simulation.

observed spontaneous hydration at the filter for the configuration [K0KKK] that disrupted direct K^+–K^+ interactions (Table 1). This is a consequence of structural distortions at this region (*SI Appendix*, Fig. S3 *C* and *D*). By averaging all water-mediated permeation events observed from [WKWKW], [KWKWK], and [K0KKK] simulations (low [K^+], $V = 750$ mV, and NBFIX), we estimated an outward conductance value of ~0.5 ± 0.2 pS. This is in line with the small outward currents (absolute and relative to WT) obtained for this variant in experiments (22). Additionally, we found two water-mediated permeation events for Na^+ in hERG1-N629D (*SI Appendix*, Fig. S6 and Movie S3). Together with the binding patterns observed for Na^+ at the SF (see below), this observation is in qualitative agreement with the lack of selectivity reported for this mutant (22).

Filter Dynamics and Accessibility to Permeant Particles.

hERG1-WT. In all MD simulations of this channel variant (*SI Appendix*, Table S1), the canonical SF configuration observed in the cryo-EM structure (Fig. 1*A*) is distorted within tens to hundreds of nanoseconds, displaying RMSD values in the range of 1.5 to 3.0 Å (*SI Appendix*, Fig. S3 *A* and *B* and Movie S1). To identify metastable states of the SF and connect structural dynamics to permeation properties of the channel, we used Markov-state analysis for the trajectories started from different initial ion configurations (Fig. 1 *C*–*E*) and similar conditions of [KCl] = 150 mM, $V = 750$ mV, and NBFIX correction (*SI Appendix*, Table S1). The backbone torsions were selected as a feature, and time-lagged independent component analysis (tICA) (47) was used for dimensionality reduction. The mapping of the first two tICA components (IC 1 and 2) shows two predominant high- and medium-density regions (*SI Appendix*, Fig. S7*A*). This tICA subspace was clustered into 100 microstates for MSM construction (*SI Appendix*, Fig. S7*A*). The calculation of relaxation times with increasing sampling periods shows marginal changes for time intervals above 2.5 ns (*SI Appendix*, Fig. S7*B*). Therefore, we used $t = 2.5$ ns as lag time for constructing a transition matrix for the MSM analysis. A clear gap between the first and the second relaxation times (*SI Appendix*, Fig. S7*C*) suggested that two-state hidden Markov model (HMM) can be used to sufficiently describe states from the selected MD trajectories (48, 49).

The resulting metastable states (Fig. 3) display the carbonyl oxygens from $_{625}$VGFG$_{628}$ or sites S3–S0 shifted off the axis of symmetry, which is reflected by the fluctuations of backbone ψ angles (*SI Appendix*, Fig. S8). The most populated metastable state (state 1, $P = 0.8$) contains contributions from the three trajectories (*SI Appendix*, Fig. S7*D*) and shows an asymmetric filter. For instance, a pair of opposite chains (A&C) constricts the permeation pathway at the level of residues G626, resulting in inter C_α–C_α distances ($d_{C\alpha–C\alpha}$) of ~5 to 6 Å (Fig. 3 and *SI Appendix*, Fig. S9*A*). In turn, the other pair (B&C) maintains the cryo-EM reference value of $d_{C\alpha–C\alpha} \sim 8$ Å at this region (Fig. 3 and *SI Appendix*, Fig. S9*C*). Both pairs of opposite chains show dilation and constriction events at the upper region, reflected by $d_{C\alpha–C\alpha}$ in the range of ~5 to 12 Å at the level of $_{627}$FG$_{628}$ (Fig. 3 and *SI Appendix*, Fig. S9 *A* and *C*). This state also shows large fluctuations for F627 side chains, indicated by the RMSD peak at 6 Å (Fig. 3 and *SI Appendix*, Fig. S10*A*). The less populated metastable state (state 2, $P = 0.2$) also displays a constricted and asymmetric filter with significant fluctuations in the F627 side-chain position (Fig. 3 and *SI Appendix*, Figs. S9 *B* and *D* and S10*A*). A distinctive feature of this state is the occlusion of the permeation pathway by a F627 side chain (Fig. 3 and *SI Appendix*, Fig. S10*A*).

The MSM analysis is indicative of a filter's conformational dynamics in the low-microsecond timescale (Fig. 3). The transitions to the most populated state 1 occur almost three times faster than transitions toward state 2 (Fig. 3). Overall, both states are essentially nonconducting. The permeant cations accumulate

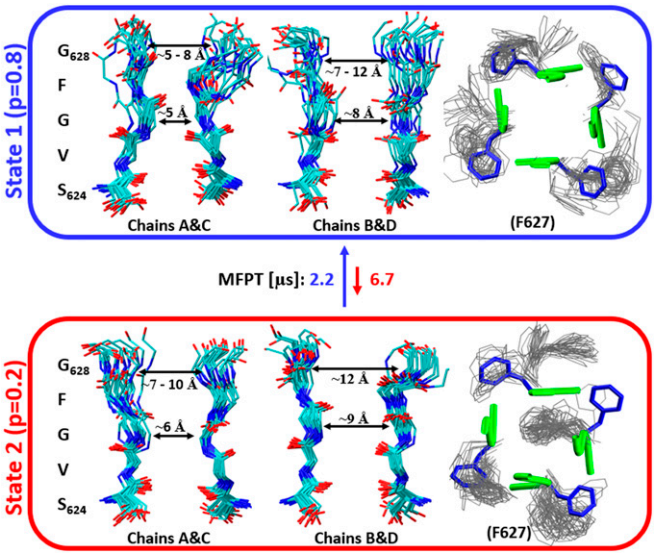

Fig. 3. Two-state HMM for the SF of hERG1-WT. The model was built using trajectories started from different ion configurations (Fig. 1 *C*–*E*), [KCl] = 150 mM, $V = 750$ mV, and the NBFIX correction for ~10 μs of combined MD simulations (*SI Appendix*, Table S1). For each metastable state (states 1 and 2), we show representative configurations of the backbone for both pairs of opposite chains (*Left* and *Middle*), where the N, C, and O atoms are colored in blue, cyan, and red, respectively. The solid double-headed arrow indicates the average distance between backbone Cα atoms at the level of residues G626 and G628. We also show the dynamics of F627 side chains (*Right*). The cryo-EM configuration of the SF backbone (blue tubes) and F627 side chains (green licorice) are shown as well. Representative configurations explored by F627 side chains along the MD trajectories are shown as gray lines. Only 20 to 50 frames are superposed for clarity. Transition kinetics between the two states is evaluated using the mean first-passage time (MFPT) metric.

below the constriction region at G626, which blocks their exit toward the extracellular side (*SI Appendix*, Fig. S11*A*). This is in line with the small number of permeation events and the long latent periods observed in our simulations for the WT channel (Fig. 2*A*). In this context, water-mediated permeation events will only occur during transient deconstriction and rehydration events at the filter lasting only tens of nanoseconds (Fig. 2*A* and Movie S1). The binding sites S0–S3 remain distorted in these transient "permeation-competent" states. The loss of binding sites at the filter of potassium channels has been shown to impair the efficiency of cation permeation (34, 50–53), which is in agreement with the small and flickering K^+-selective outward conductance observed in our simulations (see above) and experimental reports for hERG1-WT (2–5, 7).

To better understand the underpinnings of SF instability in hERG1-WT, we focused on the simulation that contributes almost equally to both metastable states ([WKWKW] initial configuration, *SI Appendix*, Fig. S7*D*). Notably, the constricted SF states show a network of hydrogen bonds within the filter itself and the surrounding regions. The former includes the interchain hydrogen bond pair F627–G626 (*SI Appendix*, Table S2), resulting from F627 backbone torsions (Fig. 4*A* and *SI Appendix*, Fig. S8). We also found a stable intrachain hydrogen bond between residues N629 (vestibule) and S620 (P-helix) (*SI Appendix*, Table S2). This interaction could be either direct ($d_{donor–acceptor} < 3.5$ Å) or water mediated ($d_{donor–acceptor} \sim 6$ Å) (*SI Appendix*, Fig. S12*A*) due to hydration present behind the SF in all simulations (Table 1 and Fig. 4 *A* and *B*). The SF interactions with S620 are also essential for stabilizing V625 carbonyl group orientation off-axis via hydrogen bonding (Fig. 4*B* and *SI Appendix*, Table S2). The analysis of several-microseconds-long all-atom MD simulations also indicate coupling between the outer-mouth vestibule and the S5–P

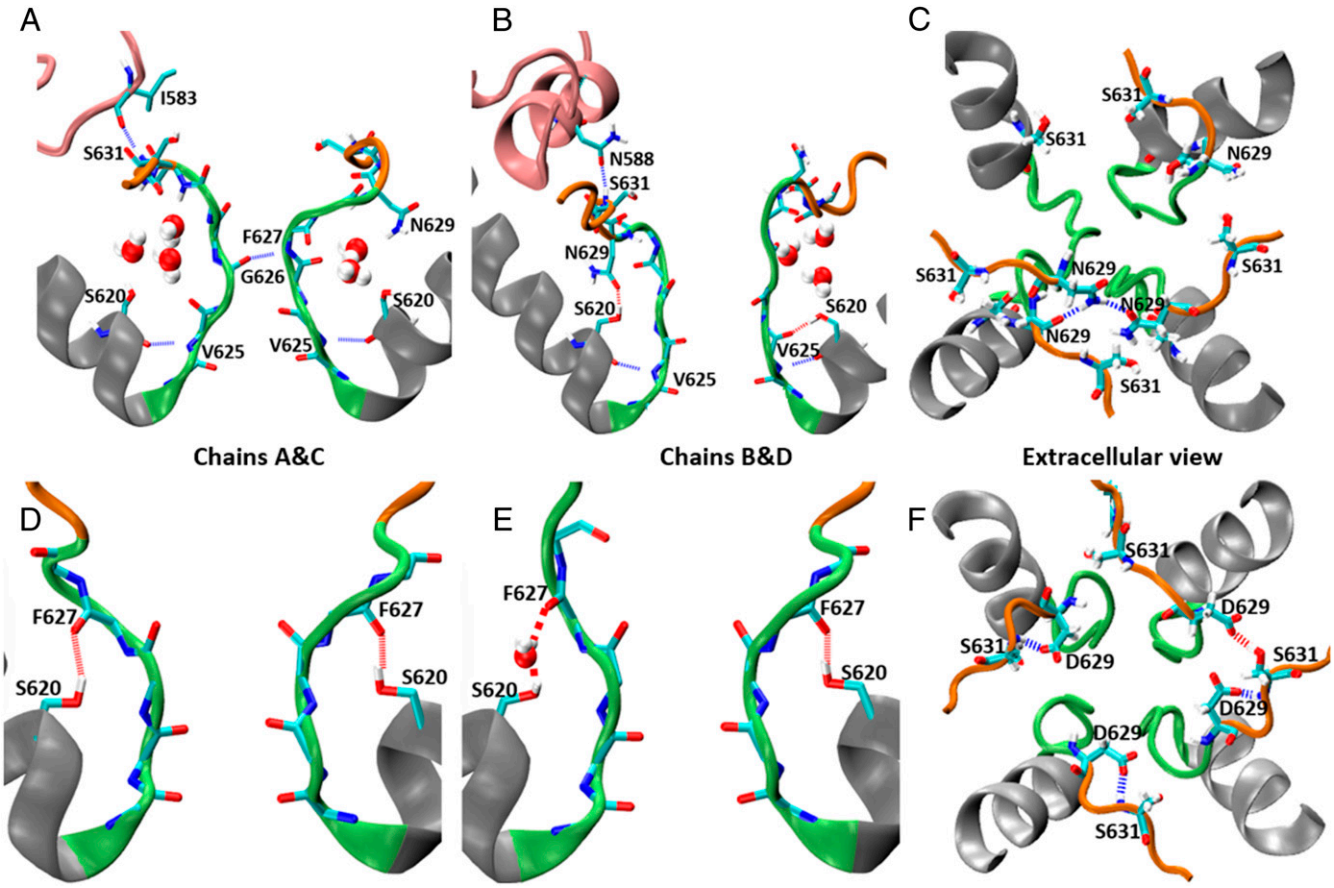

Fig. 4. Hydrogen bond networks and hydration in the vicinity of the SF of hERG1 variants. (*A*–*C*) WT and (*D*–*F*) N629D. For each channel variant, the analysis was focused on the simulation performed using the [WKWKW] configuration, $[K^+]$ = 150 mM, V = 750 mV, and the NBFIX correction (~4 μs long). *A*, *B*, *D*, and *E* show side views of the SF for each pair of opposite chains. *C* and *F* show the extracellular vestibule and SF for each hERG1 variant. The same coloring scheme as in Fig. 1 is used to highlight the structural motifs.

helices of the hERG1 channel through an extensive hydrogen-bonding network involving the pairs S631–N588 and S631–I583 (Fig. 4 *A* and *B* and *SI Appendix*, Table S2). The S5–P segments behave as highly dynamic elements of the pore domain, switching between helical and unstructured conformations (with RMSD values up to 6 Å; *SI Appendix*, Fig. S13*A*).

hERG1-N629D. The substitution N629D induced restricted backbone dynamics (RMSD ≤ 1 Å) in the simulation performed at low $[K^+]$, V = 750 mV, NBFIX correction, and [WKWKW] initial configuration (*SI Appendix*, Fig. S3 *C* and *D*). However, the simulations performed under the same conditions but using the ion configurations [KWKWK] and [K0KKK] displays larger fluctuations (RMSD up to 3 Å) at this region (*SI Appendix*, Fig. S3 *C* and *D*). These three trajectories were used to build an MSM model to identify metastable states of the SF and connect structural dynamics to permeation properties of this mutant. The mapping on the first two tICA components (IC 1 and 2) shows two predominant high- and medium- density regions (*SI Appendix*, Fig. S14*A*). This tICA subspace was clustered into 40 microstates for MSM construction (*SI Appendix*, Fig. S14*A*). The calculation of relaxation times with increasing sampling periods shows marginal changes for time intervals above 2.5 ns (*SI Appendix*, Fig. S14*B*). Therefore, a lag time of 2.5 ns was used for estimating the transition matrix. We detected a large timescale gap between the first and second relaxation timescales of the MSM (*SI Appendix*, Fig. S14*C*). Therefore, a two-state HMM was built for this variant (Fig. 5).

The most populated metastable state (state 1, P = 0.8) has contributions from the three independent trajectories (*SI Appendix*, Fig. S14*D*) and displays a mostly symmetric and nonconstricted filter as measured by diagonal distances at the level of G626 from opposing pairs of monomers ($d_{C\alpha-C\alpha}$ ~ 7 Å) (Fig. 5 and *SI Appendix*, Fig. S15 *A* and *C*). Also, both pairs of opposite chains show dilation marked by positions of $_{627}FG_{628}$ ($d_{C\alpha-C\alpha}$ ~ 14 to 16 Å), indicating the disruption of S0–S2 binding sites (Fig. 5 and *SI Appendix*, Fig. S15 *A* and *C*). This dilation promotes hydration of the vestibule in the SF and dehydration behind this region, which constitutes a reversed water occupancy pattern with respect to simulations in the WT (Table 1). Notably, this state shows restricted fluctuations for backbone ψ angles and for the F627 side chains (RMSD of ~1.0 Å) (Fig. 5 and *SI Appendix*, Figs. S10 *B* and S16). The simulation starting from water-mediated SF occupancy ([WKWKW], $[K^+]$ = 150 mM, V = 750 mV, and NBFIX) shows the largest contribution to this metastable state (*SI Appendix*, Fig. S14*D*). The filter is stabilized by the hydrogen bond network composed of the S620–F627 and S631–D629 pairs (Fig. 4 *D*–*F* and *SI Appendix*, Table S2). The restricted dynamics at the filter agree with the lack of flickering and inward rectification reported for this mutant (22).

The absence of constriction and occlusion at the SF of state 1 suggests that this a permeation-competent metastable state. Indeed, this state shows binding patterns for K^+ and Na^+ that have been observed in bacterial potassium channels (50, 54, 55). For instance, K^+ ions were found coordinated by eight carbonyl oxygens at the conserved site S3, four from each plane on the top

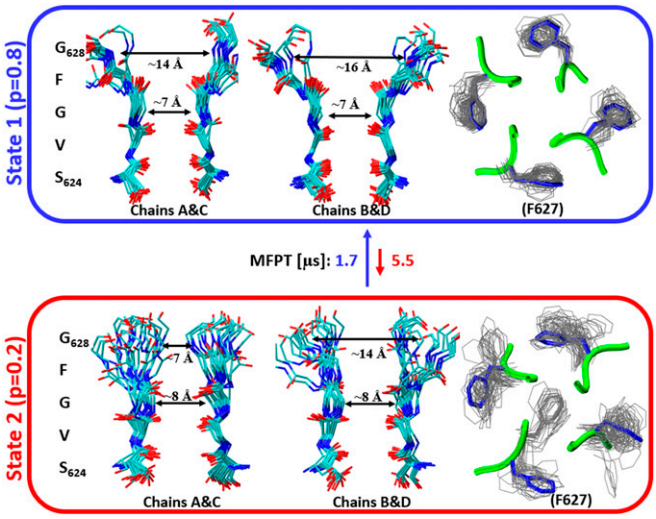

Fig. 5. Two-state HMM for the SF of hERG1-N629D. The model was built using trajectories started from different ion configurations (Fig. 1 *C–E*), [KCl] = 150 mM, V = 750 mV, and the NBFIX correction for ∼10 μs of combined MD simulations (*SI Appendix*, Table S1). For each metastable state (states 1 and 2), we show representative configurations of the backbone for both pairs of opposite chains (*Left* and *Middle*) and for F627 side chains (*Right*). We used the same coloring scheme as in Fig. 3. Only 20 to 50 frames are superposed for clarity. Transition kinetics between the two states is evaluated using the mean first-passage time (MFPT) metric.

and bottom of square-antiprism cage (*SI Appendix*, Figs. S11*B* and S17*A*). Although the cations were mostly dehydrated at S3, they transiently interact with water molecules accessing site S4, which participate in the knock-on events between cations residing at S_{cav} and S3 (*SI Appendix*, Figs. S11*B* and S17*B* and Movie S2). In turn, Na^+ ions accumulated preferentially at the planes formed by carbonyl oxygens from the S3 binding site (*SI Appendix*, Fig. S11*C*). At each plane, sodium cations were coordinated within an octahedral coordination cage formed by four carbonyl oxygen atoms and two opposing water molecules at both sides of each plane, which participated in the knock-on events between permeant Na^+ cations (*SI Appendix*, Figs. S11*C* and S17 *A* and *B* and Movie S3). Nevertheless, the number of cation permeation events in hERG1-N629D is small (see above). This suggests that the dilation and hydration of S0–S2 SF binding sites (Fig. 5) impairs the efficiency of selective cation permeation in this mutant, as reported for bacterial and mammalian channels displaying noncanonical filters (34, 50–53).

The [KWKWK] simulation contributed to the less populated metastable state (state 2, P = 0.2) (*SI Appendix*, Fig. S14*D*). This state also displays a nonconstricted filter ($d^{G626}_{C\alpha-C\alpha} \sim 8$ Å), but there is an asymmetry at the level of $_{627}FG_{628}$, showing $d_{C\alpha-C\alpha} \sim 7$ and 14 Å for chain pairs A&C and B&D, respectively (Fig. 5 and *SI Appendix*, Fig. S15 *B* and *D*). The cation binding sites S0–S3 are disrupted, as indicated by the distributions of backbone ψ angles (Fig. 5 and *SI Appendix*, Fig. S16). This simulation also displays large fluctuations for F627 side chains (RMSD ∼ 3 to 8 Å), which may occlude the permeation pathway (Fig. 5 and *SI Appendix*, Fig. S10*B*). This occluded state may be related to transient inactivated states reported for the mutant (24). The MSM analysis shows that the occlusion of the permeation pathway by F627 side chains is the rate-determining process (kinetics is in the microseconds' timescale), where transitions toward state 1 occurs almost three times faster than transitions toward state 2 (Fig. 5). This is in line, at least qualitatively, with the spontaneous recovery from inactivation and lack of inward rectification reported for this channel variant (22, 24).

Impact of the Electrolyte Concentration on the SF Dynamics in hERG1-N629D. One of the most notable features of the N629D mutant is recovery of WT-like permeation properties by the transient exposure to high extracellular K^+ concentrations (24). The results of simulations performed at physiological and high concentrations of K^+ may provide molecular mechanism for the observed effect. The electrostatic potential created by introducing negative moiety in the position 629 may function as a sensor of the extracellular electrolyte concentration. The extracellular surface near D629 shows strongly negative potential for [K^+] = 150 mM (Fig. 6*A*) that shifts toward more positive values for [K^+] = 500 mM (Fig. 6*B*). There are also significantly larger SF fluctuations after increasing [K^+] from 150 to 500 mM, especially for the replica performed using V = 500 mV (*SI Appendix*, Figs. S3 C and D and S18 *A–C*). In this replica, we observed constriction, dilation, and occlusion by F627 side chains at the filter (*SI Appendix*, Fig. S19 *A–C*). We also found a decrease in the stability of hydrogen bond pairs S620–F627 and S631–D629 at the upper region of the SF (*SI Appendix*, Table S2), which favors hydration behind this region (2 ± 1 water molecules). In contrast, there is increased stability of the hydrogen bond pairs S631–N588 and S620–V625 (*SI Appendix*, Table S2). We also observed dewetting of the SF during most of the simulation time (2 ± 1 water molecules) and low K^+ occupancy of ∼1 ± 1. A total of eight water-mediated K^+ permeation events occurred for V = 750 mV and 500 mM for this mutant (*SI Appendix*, Fig. S5*C*). Remarkably, most of these features are reminiscent of SF dynamics and permeation in the WT (see above).

Discussion

Gating Modalities at the SF of hERG1-WT. Our simulations show that K^+-selective transport in hERG1-WT is controlled by an ensemble of SF states, including constriction/dilation and dehydration/hydration events that take place under all tested conditions such as initial ion configuration, voltage, [KCl], and LJ parameters for ion–protein(backbone) interactions (*SI Appendix*, *Supplementary Results*). These observations agree with the recent work of Jekhmane et al. (25), who found a direct relationship between gating modalities and changes in the statistical weight of preexisting SF states in the KcsA channel. Notably, the asymmetrically constricted SF states we found for hERG1-WT contrasts with the symmetrically constricted SF proposed for inactivated

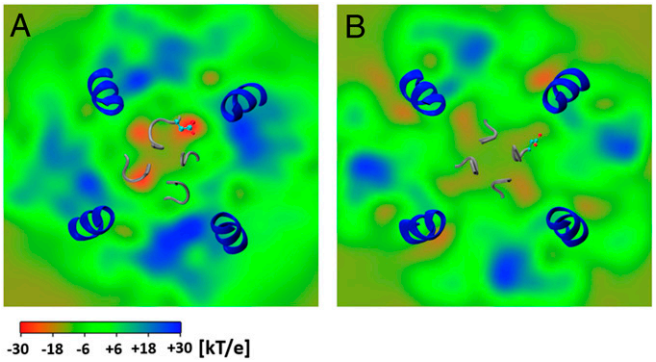

Fig. 6. Average electrostatic potential (2D) *xy* maps at *z* position of residue 629 for hERG1-N629D. The simulations were performed using [K^+] = 150 (*A*) and 500 (*B*) mM. The maps are shown perpendicular to the channel axis (cytoplasmic view). The segments of the S6 helices (blue cartoon) and the SF (gray tubes) are shown for spatial reference. Only one of the four D629 residues is shown for clarity, using ball-and-stick representation (C and O atoms are colored in cyan and red, respectively). Both simulations were performed using the [WKWKW] initial SF configuration, V = 750 mV, and the NBFIX correction. We obtained a map similar to *B* for the simulation performed using [K^+] = 500 mM and V = 500 mV (not shown).

$KcsA^{WT}$ (35, 37, 51, 56–59). Furthermore, asymmetrically constricted SF states have been linked to the inactivated state of the semisynthetic $KcsA^{D\text{-}ala77}$ channel (60). Overall, these results contrast with the notion of "well-defined" and mutually exclusive symmetrically constricted or dilated states traditionally proposed for SF-level gating in potassium channels (20, 35, 37, 51, 56–59) and suggest that SF instability is an intrinsic property of hERG1-WT. We therefore consider that the well-defined canonical binding sites observed at the filter of hERG1 cryo-EM structure (Fig. 1*A*) does not represent an inactivated state as suggested by MacKinnon and coworker (26).

Interestingly, MacKinnon and coworker (26) reported that F627 side chains display a unique configuration in hERG1 compared to the equivalent tyrosine residue in the structures of slow C-type inactivating potassium channels. The authors proposed that the dynamics of F627 side chains could be critical for fast inactivation in hERG1. Also, Massaeli et al. (61) suggested that F627 induces structural instability at the filter region of hERG1-WT. In this regard, our simulations show that the dynamics of F627 residues play a critical role in defining the metastable states obtained from our MSM models. We propose that the occlusion of the filter by these side chains could be critical for modulating the conduction properties of the filter in this channel. However, this occluded state was not equally explored by all of the MD replicas of WT and N629D variants, indicating sampling limitations. Indeed, the occlusion by F627 side chains is the slowest transition observed in both MSMs as it requires a large reorganization of the filter, which is in line with its low probability. The implied timescales for the slowest transitions between SF metastable states in our MSM model (microseconds) are still faster than ones fitted from the electrophysiological experiments assessing flickering and inactivation dynamics in hERG1-WT (tens of milliseconds) (7). However, most of the residues that we found involved in the structural framework of distorted SF states are in excellent agreement with mutagenesis experiments (see next section). We therefore suggest that the metastable states identified in our MD simulations for hERG1-WT should be regarded as early transitions involved in subsequent events linked to flickering and inactivation of I_{Kr} (2–5, 7).

Role of the Structural Motifs Around the Selectivity Filter of hERG1-WT. The stable intrachain hydrogen bond between N629 (outer-mouth vestibule) and S620 (P-helix) during constricted SF filter states agrees with the work of Köpfer et al. (62), who suggested that this interaction may function as a "switch" that triggers the collapse of the filter in hERG1-WT. A similar role has been suggested for the hydrogen bond of E71–D80 behind the SF of the bacterial counterpart KcsA (35, 37, 51, 56–59). Also, the presence of water molecules in this region that participate in the N629–S620 hydrogen bond has been deemed critical to stabilize the collapsed SF state in K^+-selective channels (25, 35, 63, 64). Additionally, S620 stabilizes the backward flipping of valine carbonyl oxygen (V625) at the SF of hERG1-WT, which has been associated with flickering currents and C-type inactivation in bacterial and mammalian K^+ channels such as KcsA (V76) (25, 35, 65–68) and hEAG1 (V437) (69), respectively. Overall, these findings agree with experimental mutagenesis studies reporting the critical role of N629 and S620 in the control of inactivation in hERG1 (22, 70–72).

The interactions found between the S5–P helices and the outer-mouth vestibule of hERG1-WT through the hydrogen bond pairs S631–N588 and S631–I583 during constricted SF states agree with the mutagenesis studies of Clarke et al. (73) and Liu et al. (74). The former study reported that residue S631 is critical for the S5–P helix to induce inactivation in hERG1. The latter found that N588C and I583C substitutions have high and intermediate impact on hERG1 inactivation, respectively. Also, the switching between helical and unstructured conformations we observed for the S5–P region is supported by previous circular dichroism and NMR studies, which suggested that these short amphipathic segments can adopt helical or random-coil configurations depending on their interaction with aqueous or hydrophobic environments, respectively (75, 76).

Additionally, there are several reasons to rule out any effect of the relaxation that takes place at the VSDs and the PD gate on the dynamics observed at the SF in our MD simulations. From the experimental perspective, mutations at the charged residues in the S4 helix of the VSDs that profoundly affect voltage-dependent activation have no effects on inactivation (31, 77). Furthermore, no direct link was found between inactivation and conformational changes in the S4 helix (78). It is also well established that hERG1 can inactivate in the closed state, before charge transfer at the VSDs and PD gate opening takes place (7). Moreover, it was recently reported that split hERG1 channels lacking a covalent link between VSDs and PD show kinetics of onset/recovery from inactivation similar to WT (32, 79). Last, previous MD simulations of homology-based structural models of the PD of hERG1 (lacking the VSDs) also displayed instabilities at the SF (62, 80, 81).

Loss of Selectivity and Phenotype Reversion in hERG1-N629D. In contrast to WT, the filter of hERG1-N629D can permeate Na^+ and displays sensitivity to the settings used in our simulations. Similar properties have been reported for bacterial sodium channels, for which the EEEE ring at the filter induces sensitivity to a myriad of conditions like cation type, cation configuration, concentration gradients, and applied voltage in simulations (49). Therefore, the sensitivity of SF dynamics to initial conditions observed in hERG1-N629D simulations could be a consequence of the ring of negative charges (DDDD) at the outer-mouth vestibule of the mutant filter.

In the context of low $[K^+]$ simulations (Fig. 7*A*), we propose that repulsive interactions among (−)D629 residues triggers widening/hydration at the SF sites S0–S2, which induces the formation of the stable hydrogen bond pairs S620–F627 (behind the filter) and S631–D629 (at the outer-mouth vestibule), and promotes dehydration behind the filter. These hydrogen bonds underpin the structural stability of the most populated metastable state (state 1) for this variant. Notably, this SF architecture (dilated vestibule at S0–S2 and conserved S3–S4 sites) is reminiscent of known bacterial and mammalian nonselective channels such as NaK and HCN, respectively (54, 55, 82). Indeed, the coordination numbers and geometries we observed for K^+ and Na^+ at the site S3 of hERG1-N629D (state 1) agree with reports for the nonselective NaK channel (50, 54, 55). Therefore, the lack of selectivity in hERG1-N629D may result from the disruption of binding sites for K^+, which has been shown to prevent efficient cation dehydration and selective binding at the filter of potassium channels (34, 50–53).

On the other hand, the screening of (−)D629 charges in high $[K^+]$ simulations would be an essential factor in shifting SF modalities from "NaK-like" (observed at low $[K^+]$) to "WT-like" (Fig. 7*B*). The decreased repulsion among (−)D629 residues would reduce the stability of hydrogen bond pairs S620–F627 and S631–D629 at the upper region of the filter. Consequently, there will be rehydration behind the SF and recovery of interaction between the extracellular vestibule of the channel and S5–P helices (through S631–N588 and S620–V625 hydrogen bonds). Hence, these events will result in constriction/dilation or dehydration/hydration events at the SF of this mutant, reminiscent of our hERG1-WT simulations. Finally, it is worth pointing out that the $[K^+]$ = 150 and 500 mM used for hERG1-N629D simulations were much higher than those used in the work of Teng et al. (external $[K^+] \leq 40$ mM) (24). However, our observations qualitatively agree with their reports regarding the rescue of WT-like SF dynamics for this mutant using higher $[K^+]$ than physiological levels. Therefore, our results support the possible therapeutic benefits of transient increases in external $[K^+]$ for

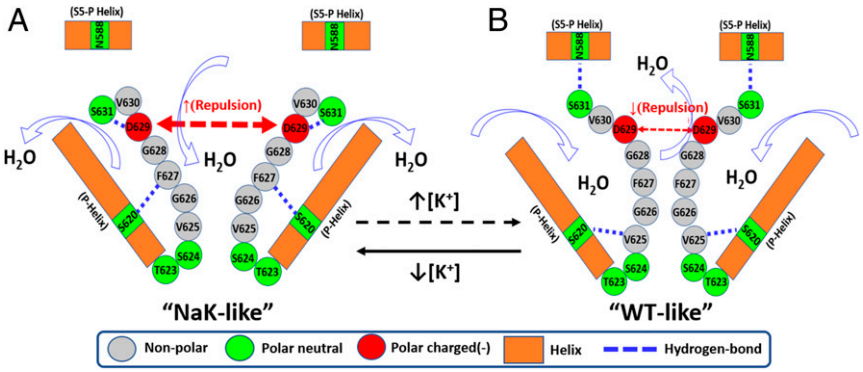

Fig. 7. Reorganization of the interaction network at the SF of hERG1-N629D. Changes in the external [K^+] modulate the repulsion among residues (−)D629 in the outer-mouth vestibule, favoring either the NaK-like configuration at low [K^+] (*A*) or WT-like configuration at high [K^+] (*B*). See *Discussion* for details.

reversing LQTS induced by N629D inherited mutation, as proposed by Teng et al. (24).

Conclusions

The results presented here are an important step toward understanding the molecular mechanisms responsible for filter-level gating and ion discrimination in physiological (WT) and pathological (N629D) hERG1 variants. The noncanonical SF in hERG1-WT ($_{626}GFGN_{629}$) is structurally unstable in simulations performed with different initial ion configurations, voltages, electrolyte concentration, and force-field corrections. The filter explores an ensemble of collapsed/dilated and dehydrated/hydrated states that allow K^+-selective permeation events in the microsecond timescale. These SF modalities result from a dynamic interaction network among residues from the filter itself, the outer-mouth vestibule, P-helices, and the S5–P segments, in agreement with mutagenesis experiments. Overall, these SF states should be regarded as early transitions involved in subsequent events linked to flickering and inactivation of I_{Kr}. In contrast to WT, the mutant SF ($_{626}GFGD_{629}$) displays sensitivity to the conditions used in the simulation. This property is induced by the ring of negative charges (DDDD) at the vestibule, which is reminiscent of the EEEE ring in the filter of bacterial Na^+-selective channels. Under low [K^+] conditions, the most populated metastable state of hERG1-N629D shows a structurally stable configuration that is reminiscent of nonselective bacterial NaK channels and allows the permeation of K^+ and Na^+ in our voltage-applied simulations. These findings are in line with the loss of inactivation and selectivity in this arrhythmogenic channel variant. Additionally, hERG1-N629D exhibits WT-like dynamics at the filter region in simulations using high [K^+]. This qualitatively agrees with the recovery of inactivation and selectivity (reversal of gain-of-function phenotype) in the mutant after exposure to higher [K^+] than physiological levels. Finally, we propose that the ring of (−)D629 charges at the outer-mouth vestibule of the mutant channel functions as an electrostatic switch, inducing NaK-like or WT-like properties of the SF depending on the electrostatic-screening effect of external [K^+].

Methods

In this work, we considered the transmembrane and C-terminal regions of the open-state cryo-EM structure of hERG1 (PDB ID code 5VA2) at 3.8-Å resolution (26) (residues 398 to 862; *SI Appendix*, Fig. S1). The membrane–protein systems for hERG1-WT and -N629 were built using the CHARMM-GUI (83–85) and embedded in a POPC lipid membrane. The CHARMM C36 force field for proteins (86) and lipids (87) along with TIP3P water model (88) was used. Furthermore, two different sets of LJ parameters describing ion–carbonyl interactions were considered (43). A constant electric field (28) E_z corresponding to transmembrane potentials (V) of +500 and ±750 mV was applied along the z direction perpendicular to the membrane to all of the atoms in the simulation box. All simulation conditions (hERG1 variants, ion species and their initial configuration at the filter, applied voltage, electrolyte concentrations, the use of the NBFIX correction, and the simulation time) are shown in *SI Appendix*, Table S1. The MD software NAMD 2.13 (89) was used to perform minimization and equilibration runs. The Python library PyEMMA was used for MSM analysis (90), using backbone torsions of the residues at the SF as features, and tICA (47) was applied for dimensionality reduction. We performed clustering on the first two tICA components. The Anton 2 software, version 1.27.0, from D. E. Shaw Research was used for production runs (2 to 4 μs) using the purpose-built Anton 2 supercomputer (91). Additional details about simulations and analysis protocols are described in *SI Appendix, Supplementary Methods*.

The data and datasets generated and analyzed in the current study can be accessed upon request sent to the corresponding authors of the manuscript.

ACKNOWLEDGMENTS. The work in S.Y.N.'s group was supported by NIH Grant R01HL128537-03); H.J.D. was supported by Canadian Institutes for Health Research Project Program Grant FRN-CIHR 156236). W.E.M. would like to acknowledge support from a Vanier Canada Graduate scholarship, a Killam scholarship, and an Alberta Innovates Health Solutions studentship. Support was also provided by the following: American Heart Association Predoctoral Fellowship 16PRE27260295 (K.R.D.) and Career Development Award 19CDA34770101 (I.V.), NIH Common Fund OT2-OD026580-01 (C.E.C. and I.V.), National Heart, Lung, and Blood Institute (NHLBI) Grant R01HL128537-03 (C.E.C.), NHLBI Grant U01HL126273-04 (C.E.C.), Extreme Science and Engineering Discovery Environment (XSEDE) Grant MCB170095 (I.V.), and University of California, Davis, Department of Physiology and Membrane Biology Research Partnership Fund (I.V. and C.E.C.). Anton 2 computer time was provided by the Pittsburgh Supercomputing Center (PSC) through Grant R01GM116961 from the NIH. The Anton 2 machine at PSC was generously made available by D. E. Shaw Research; for the grants themselves, ANTON 2 PSCA16108P and PSCA17021P (C.E.C., I.V., and S.Y.N.).

1. G. A. Gutman *et al.*; International Union of Pharmacology, International Union of Pharmacology. XLI. Compendium of voltage-gated ion channels: Potassium channels. *Pharmacol. Rev.* **55**, 583–586 (2003).
2. M. C. Trudeau, J. W. Warmke, B. Ganetzky, G. A. Robertson, HERG, a human inward rectifier in the voltage-gated potassium channel family. *Science* **269**, 92–95 (1995).
3. R. Schönherr, S. H. Heinemann, Molecular determinants for activation and inactivation of HERG, a human inward rectifier potassium channel. *J. Physiol.* **493**, 635–642 (1996).
4. P. L. Smith, T. Baukrowitz, G. Yellen, The inward rectification mechanism of the HERG cardiac potassium channel. *Nature* **379**, 833–836 (1996).
5. P. S. Spector, M. E. Curran, A. Zou, M. T. Keating, M. C. Sanguinetti, Fast inactivation causes rectification of the IKr channel. *J. Gen. Physiol.* **107**, 611–619 (1996).
6. V. Vijayvergiya, S. Acharya, J. Poulos, J. Schmidt, Single channel and ensemble hERG conductance measured in droplet bilayers. *Biomed. Microdevices* **17**, 12 (2015).
7. J. Kiehn, A. E. Lacerda, A. M. Brown, Pathways of HERG inactivation. *Am. J. Physiol.* **277**, H199–H210 (1999).
8. M. E. Curran *et al.*, A molecular basis for cardiac arrhythmia: HERG mutations cause long QT syndrome. *Cell* **80**, 795–803 (1995).
9. M. C. Sanguinetti, C. Jiang, M. E. Curran, M. T. Keating, A mechanistic link between an inherited and an acquired cardiac arrhythmia: HERG encodes the IKr potassium channel. *Cell* **81**, 299–307 (1995).
10. M. C. Sanguinetti, M. E. Curran, P. S. Spector, M. T. Keating, Spectrum of HERG K^+-channel dysfunction in an inherited cardiac arrhythmia. *Proc. Natl. Acad. Sci. U.S.A.* **93**, 2208–2212 (1996).

11. C. A. Satler, M. R. Vesely, P. Duggal, G. S. Ginsburg, A. H. Beggs, Multiple different missense mutations in the pore region of HERG in patients with long QT syndrome. *Hum. Genet.* **102**, 265–272 (1998).
12. Z. Zhou, Q. Gong, M. L. Epstein, C. T. January, HERG channel dysfunction in human long QT syndrome. Intracellular transport and functional defects. *J. Biol. Chem.* **273**, 21061–21066 (1998).
13. J. Chen, A. Zou, I. Splawski, M. T. Keating, M. C. Sanguinetti, Long QT syndrome-associated mutations in the Per-Arnt-Sim (PAS) domain of HERG potassium channels accelerate channel deactivation. *J. Biol. Chem.* **274**, 10113–10118 (1999).
14. M. T. Keating, M. C. Sanguinetti, Molecular and cellular mechanisms of cardiac arrhythmias. *Cell* **104**, 569–580 (2001).
15. V. Ruta, Y. Jiang, A. Lee, J. Chen, R. MacKinnon, Functional analysis of an archaebacterial voltage-dependent K^+ channel. *Nature* **422**, 180–185 (2003).
16. L. Gao, X. Mi, V. Paajanen, K. Wang, Z. Fan, Activation-coupled inactivation in the bacterial potassium channel KcsA. *Proc. Natl. Acad. Sci. U.S.A.* **102**, 17630–17635 (2005).
17. A. S. Thomson, B. S. Rothberg, Voltage-dependent inactivation gating at the selectivity filter of the MthK K^+ channel. *J. Gen. Physiol.* **136**, 569–579 (2010).
18. T. Hoshi, W. N. Zagotta, R. W. Aldrich, Biophysical and molecular mechanisms of Shaker potassium channel inactivation. *Science* **250**, 533–538 (1990).
19. T. Hoshi, W. N. Zagotta, R. W. Aldrich, Two types of inactivation in Shaker K^+ channels: Effects of alterations in the carboxy-terminal region. *Neuron* **7**, 547–556 (1991).
20. T. Hoshi, C. M. Armstrong, C-type inactivation of voltage-gated K^+ channels: Pore constriction or dilation? *J. Gen. Physiol.* **141**, 151–160 (2013).
21. Q. Gong, C. L. Anderson, C. T. January, Z. Zhou, Role of glycosylation in cell surface expression and stability of HERG potassium channels. *Am. J. Physiol. Heart Circ. Physiol.* **283**, H77–H84 (2002).
22. J. P. Lees-Miller, Y. Duan, G. Q. Teng, K. Thorstad, H. J. Duff, Novel gain-of-function mechanism in K^+ channel-related long-QT syndrome: Altered gating and selectivity in the HERG1 N629D mutant. *Circ. Res.* **86**, 507–513 (2000).
23. G. Q. Teng *et al*., Homozygous missense N629D hERG (KCNH2) potassium channel mutation causes developmental defects in the right ventricle and its outflow tract and embryonic lethality. *Circ. Res.* **103**, 1483–1491 (2008).
24. G. Q. Teng *et al*., $[K^+]_o$-dependent change in conformation of the HERG1 long QT mutation N629D channel results in partial reversal of the *in vitro* disease phenotype. *Cardiovasc. Res.* **57**, 642–650 (2003).
25. S. Jekhmane *et al*., Shifts in the selectivity filter dynamics cause modal gating in K^+ channels. *Nat. Commun.* **10**, 123 (2019).
26. W. Wang, R. MacKinnon, Cryo-EM structure of the open human ether-a-go-go-related K^+ channel HERG. *Cell* **169**, 422–430.e10 (2017).
27. D. Naranjo, H. Moldenhauer, M. Pincuntureo, I. Díaz-Franulic, Pore size matters for potassium channel conductance. *J. Gen. Physiol.* **148**, 277–291 (2016).
28. B. Roux, The membrane potential and its representation by a constant electric field in computer simulations. *Biophys. J.* **95**, 4205–4216 (2008).
29. J. H. Prinz *et al*., Markov models of molecular kinetics: Generation and validation. *J. Chem. Phys.* **134**, 174105 (2011).
30. J. H. Prinz, J. D. Chodera, F. Noé, Estimation and validation of Markov models. *Adv. Exp. Med. Biol.* **797**, 45–60 (2014).
31. M. Zhang, J. Liu, G. N. Tseng, Gating charges in the activation and inactivation processes of the HERG channel. *J. Gen. Physiol.* **124**, 703–718 (2004).
32. P. de la Peña, P. Domínguez, F. Barros, Gating mechanism of Kv11.1 (hERG) K^+ channels without covalent connection between voltage sensor and pore domains. *Pflugers Arch.* **470**, 517–536 (2018).
33. R. N. Subbiah, M. Kondo, T. J. Campbell, J. I. Vandenberg, Tryptophan scanning mutagenesis of the HERG K^+ channel: The S4 domain is loosely packed and likely to be lipid exposed. *J. Physiol.* **569**, 367–379 (2005).
34. W. Kopec *et al*., Direct knock-on of desolvated ions governs strict ion selectivity in K^+ channels. *Nat. Chem.* **10**, 813–820 (2018).
35. J. Li, J. Ostmeyer, L. G. Cuello, E. Perozo, B. Roux, Rapid constriction of the selectivity filter underlies C-type inactivation in the KcsA potassium channel. *J. Gen. Physiol.* **150**, 1408–1420 (2018).
36. J. H. Morais-Cabral, Y. Zhou, R. MacKinnon, Energetic optimization of ion conduction rate by the K^+ selectivity filter. *Nature* **414**, 37–42 (2001).
37. Y. Zhou, J. H. Morais-Cabral, A. Kaufman, R. MacKinnon, Chemistry of ion coordination and hydration revealed by a K^+ channel-Fab complex at 2.0 Å resolution. *Nature* **414**, 43–48 (2001).
38. Y. Zhou, R. MacKinnon, The occupancy of ions in the K^+ selectivity filter: Charge balance and coupling of ion binding to a protein conformational change underlie high conduction rates. *J. Mol. Biol.* **333**, 965–975 (2003).
39. M. Zhou, R. MacKinnon, A mutant KcsA K^+ channel with altered conduction properties and selectivity filter ion distribution. *J. Mol. Biol.* **338**, 839–846 (2004).
40. C. Tilegenova *et al*., Structure, function, and ion-binding properties of a K^+ channel stabilized in the 2,4-ion-bound configuration. *Proc. Natl. Acad. Sci. U.S.A.* **116**, 16829–16834 (2019).
41. D. A. Köpfer *et al*., Ion permeation in K^+ channels occurs by direct Coulomb knock-on. *Science* **346**, 352–355 (2014).
42. S. Bernèche, B. Roux, Energetics of ion conduction through the K^+ channel. *Nature* **414**, 73–77 (2001).
43. S. Y. Noskov, S. Bernèche, B. Roux, Control of ion selectivity in potassium channels by electrostatic and dynamic properties of carbonyl ligands. *Nature* **431**, 830–834 (2004).
44. J. Yoo, A. Aksimentiev, New tricks for old dogs: Improving the accuracy of biomolecular force fields by pair-specific corrections to non-bonded interactions. *Phys. Chem. Chem. Phys.* **20**, 8432–8449 (2018).
45. K. R. DeMarco, S. Bekker, I. Vorobyov, Challenges and advances in atomistic simulations of potassium and sodium ion channel gating and permeation. *J. Physiol.* **597**, 679–698 (2019).
46. M. O. Jensen, V. Jogini, M. P. Eastwood, D. E. Shaw, Atomic-level simulation of current-voltage relationships in single-file ion channels. *J. Gen. Physiol.* **141**, 619–632 (2013).
47. G. Pérez-Hernández, F. Paul, T. Giorgino, G. De Fabritiis, F. Noé, Identification of slow molecular order parameters for Markov model construction. *J. Chem. Phys.* **139**, 015102 (2013).
48. F. Noé, H. Wu, J. H. Prinz, N. Plattner, Projected and hidden Markov models for calculating kinetics and metastable states of complex molecules. *J. Chem. Phys.* **139**, 184114 (2013).
49. S. Furini, C. Domene, Ion-triggered selectivity in bacterial sodium channels. *Proc. Natl. Acad. Sci. U.S.A.* **115**, 5450–5455 (2018).
50. S. Y. Noskov, B. Roux, Importance of hydration and dynamics on the selectivity of the KcsA and NaK channels. *J. Gen. Physiol.* **129**, 135–143 (2007).
51. W. W. Cheng, J. G. McCoy, A. N. Thompson, C. G. Nichols, C. M. Nimigean, Mechanism for selectivity-inactivation coupling in KcsA potassium channels. *Proc. Natl. Acad. Sci. U.S.A.* **108**, 5272–5277 (2011).
52. S. Furini, C. Domene, Nonselective conduction in a mutated NaK channel with three cation-binding sites. *Biophys. J.* **103**, 2106–2114 (2012).
53. Y. Wang, A. C. Chamberlin, S. Y. Noskov, Molecular strategies to achieve selective conductance in NaK channel variants. *J. Phys. Chem. B* **118**, 2041–2049 (2014).
54. A. Alam, Y. Jiang, Structural analysis of ion selectivity in the NaK channel. *Nat. Struct. Mol. Biol.* **16**, 35–41 (2009).
55. N. Shi, S. Ye, A. Alam, L. Chen, Y. Jiang, Atomic structure of a Na^+- and K^+-conducting channel. *Nature* **440**, 570–574 (2006).
56. J. F. Cordero-Morales *et al*., Molecular determinants of gating at the potassium-channel selectivity filter. *Nat. Struct. Mol. Biol.* **13**, 311–318 (2006).
57. J. F. Cordero-Morales *et al*., Molecular driving forces determining potassium channel slow inactivation. *Nat. Struct. Mol. Biol.* **14**, 1062–1069 (2007).
58. L. G. Cuello *et al*., Structural basis for the coupling between activation and inactivation gates in K^+ channels. *Nature* **466**, 272–275 (2010).
59. L. G. Cuello, D. M. Cortes, E. Perozo, The gating cycle of a K^+ channel at atomic resolution. *eLife* **6**, e28032 (2017).
60. J. Li *et al*., Chemical substitutions in the selectivity filter of potassium channels do not rule out constricted-like conformations for C-type inactivation. *Proc. Natl. Acad. Sci. U.S.A.* **114**, 11145–11150 (2017).
61. H. Massaeli, J. Guo, J. Xu, S. Zhang, Extracellular K^+ is a prerequisite for the function and plasma membrane stability of HERG channels. *Circ. Res.* **106**, 1072–1082 (2010).
62. D. A. Köpfer *et al*., A molecular switch driving inactivation in the cardiac K^+ channel HERG. *PLoS One* **7**, e41023 (2012).
63. S. Chakrapani *et al*., On the structural basis of modal gating behavior in K^+ channels. *Nat. Struct. Mol. Biol.* **18**, 67–74 (2011).
64. J. Ostmeyer, S. Chakrapani, A. C. Pan, E. Perozo, B. Roux, Recovery from slow inactivation in K^+ channels is controlled by water molecules. *Nature* **501**, 121–124 (2013).
65. I. H. Shrivastava, D. P. Tieleman, P. C. Biggin, M. S. Sansom, K^+ versus Na^+ ions in a K channel selectivity filter: A simulation study. *Biophys. J.* **83**, 633–645 (2002).
66. S. Bernèche, B. Roux, A gate in the selectivity filter of potassium channels. *Structure* **13**, 591–600 (2005).
67. D. Medovoy, E. Perozo, B. Roux, Multi-ion free energy landscapes underscore the microscopic mechanism of ion selectivity in the KcsA channel. *Biochim. Biophys. Acta* **1858**, 1722–1732 (2016).
68. E. Montoya *et al*., Differential binding of monovalent cations to KcsA: Deciphering the mechanisms of potassium channel selectivity. *Biochim. Biophys. Acta Biomembr.* **1859**, 779–788 (2017).
69. H. Bernsteiner, M. Bründl, A. Stary-Weinzinger, Dynamics of the EAG1 K^+ channel selectivity filter assessed by molecular dynamics simulations. *Biochem. Biophys. Res. Commun.* **484**, 107–112 (2017).
70. E. Ficker, W. Jarolimek, J. Kiehn, A. Baumann, A. M. Brown, Molecular determinants of dofetilide block of HERG K^+ channels. *Circ. Res.* **82**, 386–395 (1998).
71. I. M. Herzberg, M. C. Trudeau, G. A. Robertson, Transfer of rapid inactivation and sensitivity to the class III antiarrhythmic drug E-4031 from HERG to M-eag channels. *J. Physiol.* **511**, 3–14 (1998).
72. E. Ficker, W. Jarolimek, A. M. Brown, Molecular determinants of inactivation and dofetilide block in ether a-go-go (EAG) channels and EAG-related K^+ channels. *Mol. Pharmacol.* **60**, 1343–1348 (2001).
73. C. E. Clarke *et al*., Effect of S5P alpha-helix charge mutants on inactivation of hERG K+ channels. *J. Physiol.* **573**, 291–304 (2006).
74. J. Liu, M. Zhang, M. Jiang, G. N. Tseng, Structural and functional role of the extracellular s5-p linker in the HERG potassium channel. *J. Gen. Physiol.* **120**, 723–737 (2002).
75. A. M. Torres *et al*., Structure of the HERG K^+ channel S5P extracellular linker: Role of an amphipathic alpha-helix in C-type inactivation. *J. Biol. Chem.* **278**, 42136–42148 (2003).
76. M. Jiang *et al*., Dynamic conformational changes of extracellular S5-P linkers in the hERG channel. *J. Physiol.* **569**, 75–89 (2005).
77. R. N. Subbiah *et al*., Molecular basis of slow activation of the human ether-a-go-go related gene potassium channel. *J. Physiol.* **558**, 417–431 (2004).
78. Z. Es-Salah-Lamoureux, R. Fougere, P. Y. Xiong, G. A. Robertson, D. Fedida, Fluorescence-tracking of activation gating in human ERG channels reveals rapid S4 movement and slow pore opening. *PLoS One* **5**, e10876 (2010).
79. É. Lörinczi *et al*., Voltage-dependent gating of KCNH potassium channels lacking a covalent link between voltage-sensing and pore domains. *Nat. Commun.* **6**, 6672 (2015).

80. P. J. Stansfeld *et al*., Insight into the mechanism of inactivation and pH sensitivity in potassium channels from molecular dynamics simulations. *Biochemistry* **47**, 7414–7422 (2008).
81. L. Ceccarini, M. Masetti, A. Cavalli, M. Recanatini, Ion conduction through the hERG potassium channel. *PLoS One* **7**, e49017 (2012).
82. C. H. Lee, R. MacKinnon, Structures of the human HCN1 hyperpolarization-activated channel. *Cell* **168**, 111–120.e11 (2017).
83. S. Jo, T. Kim, W. Im, Automated builder and database of protein/membrane complexes for molecular dynamics simulations. *PLoS One* **2**, e880 (2007).
84. S. Jo, T. Kim, V. G. Iyer, W. Im, CHARMM-GUI: A web-based graphical user interface for CHARMM. *J. Comput. Chem.* **29**, 1859–1865 (2008).
85. J. Lee *et al*., CHARMM-GUI input generator for NAMD, GROMACS, AMBER, OpenMM, and CHARMM/OpenMM simulations using the CHARMM36 additive force field. *J. Chem. Theory Comput.* **12**, 405–413 (2016).
86. R. B. Best *et al*., Optimization of the additive CHARMM all-atom protein force field targeting improved sampling of the backbone φ, ψ and side-chain $\chi(1)$ and $\chi(2)$ dihedral angles. *J. Chem. Theory Comput.* **8**, 3257–3273 (2012).
87. J. B. Klauda *et al*., Update of the CHARMM all-atom additive force field for lipids: Validation on six lipid types. *J. Phys. Chem. B* **114**, 7830–7843 (2010).
88. W. Jorgensen, J. Chandrasekhar, J. Madura, M. Klein, Comparison of simple potential functions for simulating liquid water. *J. Chem. Phys.* **79**, 926–935 (1983).
89. L. Kale *et al*., NAMD2: Greater scalability for parallel molecular dynamics. *J. Comput. Phys.* **151**, 283–312 (1999).
90. M. K. Scherer *et al*., PyEMMA 2: A software package for estimation, validation, and analysis of Markov models. *J. Chem. Theory Comput.* **11**, 5525–5542 (2015).
91. D. E. Shaw *et al*., "Anton 2: Raising the bar for performance and programmability in a special-purpose molecular dynamics supercomputer" in *SC 14: Proceedings of the International Conference for High Performance Computing, Networking, Storage and Analysis* (IEEE, 2014), pp. 41–53.